

ON THE DIFFUSE LYMAN-ALPHA HALO AROUND LYMAN-ALPHA EMITTING GALAXIES

ETHAN LAKE¹, ZHENG ZHENG¹, RENYUE CEN², RAPHAEL SADOUN¹, RIEKO MOMOSE³, AND MASAMI OUCHI^{3,4}

(Dated: July 24, 2022)
Draft, 20150202

ABSTRACT

Ly α photons scattered by neutral hydrogen atoms in the circumgalactic media or produced in the halos of star-forming galaxies are expected to lead to extended Ly α emission around galaxies. Such low surface brightness Ly α halos (LAHs) have been detected by stacking Ly α images of high-redshift star-forming galaxies. We study the origin of LAHs by performing Ly α radiative transfer modeling of nine $z = 3.1$ Lyman-Alpha Emitters (LAEs) in a high resolution hydrodynamic galaxy formation simulation. We develop a method of computing the mean Ly α surface brightness profile of each LAE by effectively integrating over many different observing directions. Without adjusting any parameters, our model yields an average Ly α surface brightness profile in remarkable agreement with observations. We find that observed LAHs can not be accounted for solely by photons originating from the central LAE and scattered to large radii by hydrogen atoms in the circumgalactic gas. Instead, Ly α emission from regions in the outer halo is primarily responsible for producing the extended LAHs seen in observations, which potentially includes both star-forming and cooling radiation. The contribution from star formation in the outer halo regions can be strongly constrained to be negligible by the observed absence of an extended ultra-violet (UV) halo. Our results therefore suggest that cooling radiation from the outer halo regions of LAEs plays a major role in forming their extended LAHs. We discuss the implications and caveats of such a picture.

Subject headings: cosmology: observations — galaxies: high-redshift — radiative transfer — scattering — intergalactic medium

1. INTRODUCTION

The Ly α line is an important cosmological tool for studying star-forming galaxies in the young universe, and has been found to aid in the detection of high redshift galaxies (Rhoads et al. 2003; Ouchi et al. 2008; Gawiser et al. 2007; Guaita et al. 2010). As ionizing photons are emitted from young stars, they ionize neutral hydrogen in the surrounding interstellar medium, and are likely to be re-emitted as Ly α photons following recombination (Partridge & Peebles 1967). After they escape the interstellar medium surrounding their parent stars, they are predicted to undergo resonant scattering with neutral hydrogen gas in the surrounding medium as a result of the radiative transfer process, diffusing out both spatially and in frequency (Zheng et al. 2011a). As such, extended halos of neutral hydrogen around these Ly α emitters (LAEs) are predicted to be illuminated by scattered Ly α photons.

Many theoretical studies have predicted the existence of these so-called Ly α halos (LAHs) around high redshift galaxies (Tasitsiomi 2006; Verhamme et al. 2008; Schaefer & Verhamme 2008; Zheng et al. 2010, 2011a; Dijkstra & Kramer 2012). While these LAHs are predicted to generally be too faint to be detected on an individual basis at $z \geq 2$, their presence can be revealed

by stacking tens to hundreds of narrow band images of high redshift LAEs (Fynbo et al. 2003; Steidel et al. 2011; Zheng et al. 2011a; Matsuda et al. 2012; Momose et al. 2014). Although observationally there seems to be a consensus in favor of their existence, there are also reports of null detections of LAHs. Feldmeier et al. (2013) find marginal evidence and no evidence of LAHs for $z \sim 3.1$ and $z \sim 2.1$ LAEs, while Jiang et al. (2013) find evidence of LAHs based on results using stacked images of LAEs at redshifts of 5.7 and 6.6. Such contradicting results may be caused by small number statistics or unknown systematics (Momose et al. 2014).

The shape and size of LAHs can yield insights into the spatial distribution and kinematic properties of the circumgalactic and intergalactic medium surrounding LAEs (Zheng et al. 2011a). The shape can also be used to constrain cosmic reionization, with reionization leading to steeper surface brightness profiles (Jeeson-Daniel et al. 2012). Detailed theoretical studies of LAHs can help in understanding their origin and properties.

The aim of this paper is to apply a Monte Carlo radiative transfer code (Zheng & Miralda-Escudé 2002) to study diffuse Ly α halos surrounding $z \sim 3.1$ star-forming galaxies in a high-resolution galaxy formation simulation. By comparing with observational data, we hope to gain insight about the origin and composition of these diffuse LAHs.

This paper is divided into several sections. In Section 2, we describe the modeling method and the construction of the average Ly α surface brightness profile for each model LAE. Our main analyses and results are presented in Section 3, with comparisons to observations. In particular, Figure 8 shows the result that leads to our main conclusions. Finally, we summarize our results and

¹ Department of Physics and Astronomy, University of Utah, 115 South 1400 East, Salt Lake City, UT 84112, USA; ethan.lake@utah.edu, zhengzheng@astro.utah.edu

² Princeton University Observatory, Princeton, NJ 08544, USA

³ Institute for Cosmic Ray Research, The University of Tokyo, 5-1-5 Kashiwanoha, Kashiwa, Chiba 277-8583, Japan

⁴ Kavli Institute for the Physics and Mathematics of the Universe (WPI), The University of Tokyo, 5-1-5 Kashiwanoha, Kashiwa, Chiba 277-8583, Japan

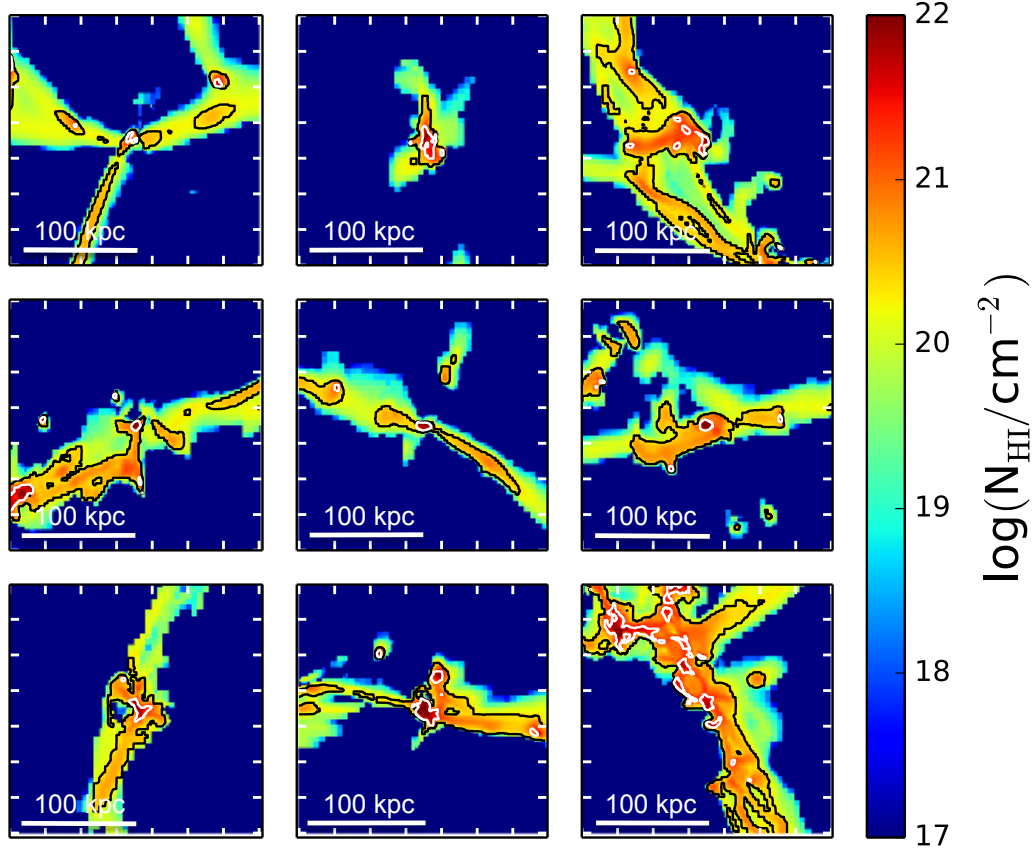


FIG. 1.— Neutral hydrogen column density maps for the model LAEs in our analysis. Each image is 224kpc (physical) on a side. The column density is computed by integrating over the whole box along the line of sight (224kpc physical). The black contours are drawn at $10^{20.3}\text{cm}^{-2}$, within which are regions corresponding to DLAs. The white contours are drawn at $10^{21.3}\text{cm}^{-2}$. Extended filamentary structures of neutral hydrogen are seen, which are connected to the extended Ly α emission discussed in this paper.

discuss the implications in Section 4.

2. MODEL

2.1. Ly α Radiative Transfer Modeling of Simulated Star-forming Galaxies

Our Ly α radiative transfer modeling of simulated star-forming galaxies is based on a cosmological simulation with the adaptive mesh refinement (AMR) Eulerian hydro code Enzo (Bryan & Norman 2000; Joung et al. 2009), as detailed in Cen (2012) and Cen & Zheng (2013). In brief, a region of comoving size $21 \times 24 \times 20h^{-3}\text{Mpc}^3$ in a low-resolution simulation (with a box size of $120h^{-1}\text{Mpc}$ comoving on a side) is chosen to be resimulated at high resolution. The resimulation has a dark matter particle mass of $1.3 \times 10^7h^{-1}M_\odot$ and the mesh refinement ensures a spatial resolution better than $11h^{-1}\text{pc}$ (physical). The resimulation includes an ionizing ultra-violet (UV) background and the self-shielding of the gas, metallicity-dependent radiative cooling, molecular hydrogen formation, star formation, and supernova feedback. The mass of a star particle is typically $\sim 10^6M_\odot$. The simulation assumes a spatially flat Λ CDM model with the following cosmological parameters: $\Omega_m = 0.28$, $\Omega_b = 0.046$, $H_0 = 100h\text{km s}^{-1}\text{Mpc}^{-1}$ with $h = 0.70$, $\sigma_8 = 0.82$, and $n_s = 0.96$.

The simulation has been used to study the kinematic properties traced by unsaturated metal lines in damped Ly α systems, which is in good agreement with observa-

tions (Cen 2012). The simulation has also been applied to study the partition of stellar light into optical and infrared light (Cen 2011). In Cen & Zheng (2013), a model of Ly α blobs (LABs) is developed based on Ly α radiative transfer modeling of the simulated star-forming galaxies in massive halos, and the observed relation between Ly α luminosity and LAB size and LAB luminosity function at $z \sim 3.1$ have been successfully reproduced. In this paper, we select from the simulation 9 $z = 3.1$ star-forming galaxies in halos of mass $10^{11.5}M_\odot$ to study the properties of LAHs associated with them. The value of $10^{11.5}M_\odot$ is chosen as a starting point for our analysis, and is within current constraints on LAE halo mass of $10^{11\pm1}M_\odot$ (Ouchi et al. 2010). The mean stellar mass of these nine galaxies is about $2.9 \times 10^{10}M_\odot$.

We implement a Monte Carlo code developed by Zheng & Miralda-Escudé (2002) for the Ly α radiative transfer calculation in extended neutral hydrogen distributions surrounding our simulated LAEs. This code has been applied to study LAEs and LABs (e.g., Zheng et al. 2010, 2011b,a; Cen & Zheng 2013; Zheng & Wallace 2014). For each galaxy, we store the relevant quantities from the simulation in a uniform cubic grid of $4R_{\text{vir}}$ on a side, with cell size 319 pc (physical, corresponding to $0.04''$). Here R_{vir} is the virial radius of the host halo, which is about 56 kpc (physical). The quantities include the Ly α luminosity, neutral hydrogen density, temperature, and velocity. The Ly α luminosity is

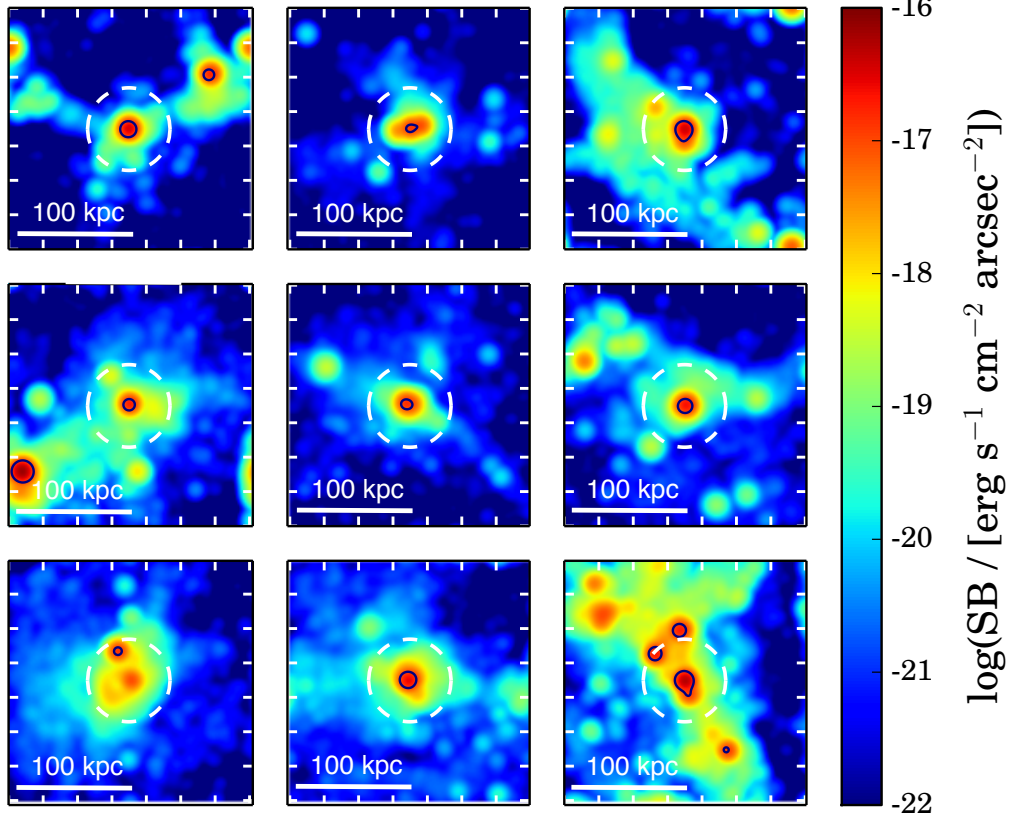


FIG. 2.— Ly α surface brightness images for all nine model LAEs in our analysis. Each image is 224 kpc (physical) on a side and has been smoothed by a 2D Gaussian kernel with a FWHM of 1.32'' to match the observation setup. Isophotal contours are drawn in black at the limit of observational detection, $10^{-17} \text{ erg s}^{-1} \text{ cm}^{-2} \text{ arcsec}^{-2}$. The dashed circle in each panel has a radius of 40 kpc, beyond which the systematic effects in the image stacking analysis in Momose et al. (2014) start to become important. The images show a rich diversity in structure at surface brightness levels below the detection threshold, which contributes to the extended LAHs.

separated into star-formation and cooling contributions. The Ly α luminosity from star formation is computed as $L_{\text{Ly}\alpha} = 10^{42}[\text{SFR}/(M_{\odot} \text{yr}^{-1})] \text{ erg s}^{-1}$ (Furlanetto et al. 2005), where SFR is the star formation rate in the cell. The Ly α luminosity from cooling radiation is computed from the de-excitation rate, which depends on neutral hydrogen density and temperature that are computed self-consistently by following the relevant species in a non-equilibrium fashion.

Each photon launched from a cell is assigned a weighted Ly α luminosity, which allows us to reproduce the total Ly α luminosity of the cell. The scatterings of the photon with neutral hydrogen atoms on its way out and the corresponding changes in position, direction, and frequency are tracked until it escapes the grid boundary. We record the initial position of each photon, the position of the last scattering, the direction and frequency after the last scattering, and the fractional contribution of cooling radiation to its total luminosity. This information is used to compute a mean surface brightness profile for each LAE, averaged over all directions (see § 2.2).

At each scattering, we also compute the escape probability towards a fixed direction and collect the escaping Ly α photons onto an integral-field-unit-like 3-dimensional array with pixel size the same as the cell size, which allows us to construct a Ly α image of each LAE as viewed along the chosen direction (Zheng & Miralda-

Escudé 2002).

Finally, we account for the effects of the intergalactic medium (IGM) outside of the box and the interstellar medium (ISM) in star-forming regions on Ly α emission, following the approximate methods in Cen & Zheng (2013). In brief, for each photon escaping the box at frequency ν , we calculate the scattering optical depth τ_{ν} from the edge of the box to an observer at $z = 0$ and apply a factor of $e^{-\tau_{\nu}}$ correction for the IGM absorption. We also apply an effective ISM dust attenuation to the intrinsic Ly α emission by applying a simple $e^{-\tau}$ model with $\tau = 0.2[\text{SFR}/(M_{\odot} \text{yr}^{-1})]^{0.6}$, motivated by observational trends of higher dust attenuation in galaxies with higher SFR (Brinchmann et al. 2004; Zahid et al. 2013). Our methods of applying IGM and ISM absorption are the same as adopted in Cen & Zheng (2013), in which the LAB luminosity function and luminosity-size relation have been successfully reproduced. In our current work of LAHs, we do not adjust any parameters and simply use the direct outputs of the radiative transfer model to compare to observations.

We show in Figure 1 the column density distribution of neutral hydrogen gas around each of our model LAEs, viewed from a fixed direction. The black contour curves are drawn at $10^{20.3} \text{ cm}^{-2}$, delineating regions corresponding to damped Ly α systems (DLAs). DLAs represent regions extremely opaque to Ly α photons, while Ly α pho-

tons can be significantly scattered in regions of much lower column densities (e.g., $> 10^{15} \text{ cm}^{-2}$). The images reveal extended, filamentary structures of neutral hydrogen connecting regions of high column densities. Scatterings of Ly α photons off hydrogen atoms in these structures leave signatures in the resulting Ly α surface brightness distributions.

Figure 2 shows the corresponding Ly α images of the nine LAEs in our analysis. The isophotal contours in each image correspond to $10^{-17} \text{ erg s}^{-1} \text{ cm}^{-2} \text{ arcsec}^{-2}$, about the surface brightness threshold for detecting individual $z \sim 3.1$ LAEs (Ouchi et al. 2008). These images reveal a rich degree of structures and a variety of morphologies at fainter surface brightness levels, which allows the LAHs to be revealed by the stacking analysis. The surface brightness distribution depends on the viewing angle (e.g. Zheng et al. 2010). The stacked image (as in Momose et al. 2014) for a sample of LAEs comes from averaging many images from galaxies of random orientations. For the relatively small number of galaxies modeled here, we can form the mean surface brightness distribution by viewing each galaxy from many different observing directions.

2.2. Computing the Mean Ly α Surface Brightness Profiles of Model LAEs

First, let us consider an observer located along a direction \mathbf{k} from one of our model galaxies. The average surface brightness $\text{SB}(R, \mathbf{k})$ at a projected radius R (physical) to the galaxy center as seen by the observer can be computed as (assuming a spatially flat universe)

$$\text{SB}(R, \mathbf{k}) = \frac{\Delta L(1+z)^{-2}}{\Delta \Omega D_c^2 [A(1+z)^2/D_c^2]}, \quad (1)$$

where $\Delta \Omega$ is a small solid angle centered around \mathbf{k} , $A \equiv \pi R \Delta R$ is the area of a small annulus around R , and ΔL is the total luminosity of escaped Ly α photons falling into $\Delta \Omega$ and with projected last scattering position within A . The quantity $\Delta L(1+z)^{-2}/(\Delta \Omega D_c^2)$ is the corresponding flux ($\text{erg s}^{-1} \text{ cm}^{-2}$) the observer at a comoving distance D_c receives, with the two factors of $1+z$ from energy redshift and time dilation. The quantity $A(1+z)^2/D_c^2$ is the solid angle extended by the annulus, seen by the observer, with the $(1+z)^2$ factor converting physical area to comoving.

The surface brightness profile at projected radius R averaged over all observing directions is then

$$\langle \text{SB}(R) \rangle = \frac{1}{4\pi} \int \text{SB}(R, \mathbf{k}) d\Omega. \quad (2)$$

Given Equation (1), for the annulus at a given R and ΔR , we only need to obtain the average of $\Delta L/\Delta \Omega$ over all observing directions for computing the integral in Equation (2). Denoting the total Ly α luminosity from this annulus as L_A , we then have $L_A = \int \Delta L/\Delta \Omega d\Omega$. In the limit of an infinite number of observing directions, we obtain

$$\langle \text{SB}(R) \rangle = \frac{L_A}{4\pi A(1+z)^4}. \quad (3)$$

This equation is the basis of computing the mean Ly α surface brightness profile for each model LAE, along with the information we record for the escaping Ly α

photons. For the mean Ly α surface brightness at projected radius R , instead of producing images viewed from many directions, we only need to obtain the sum of the total Ly α luminosity L_A for photons whose projected radii fall into the annulus around R ($R \pm \Delta R/2$ with an area A). The projected radius R_γ of a photon is computed from its escaping direction \mathbf{k}_γ and its position of last scattering \mathbf{r}_{ls} (with respect to the galaxy center) as $R_\gamma = \sqrt{r_{ls}^2 - (\mathbf{k}_\gamma \cdot \mathbf{r}_{ls})^2}$. We have verified that the method gives the same results as that from averaging images over many observational directions.

Our simulation has a much higher resolution (cell size of $\sim 0.04''$) than the observation in Momose et al. (2014). To mimic the smoothing effect in the images of Momose et al. (2014), we obtain the final surface brightness profile by convolving the resulting Ly α image with a 2D Gaussian kernel with a full width at half maximum (FWHM) of $1.32''$, corresponding to 10.3 kpc (physical) at $z = 3.1$.

3. RESULTS

We first present the results on the mean Ly α surface brightness profile in our model. We then decompose the mean profile in various ways to study its origin. Finally, we use the UV profile to further constrain the relative contributions of cooling and star-forming emission.

3.1. The Mean Ly α Surface Brightness Profile

The left panel of Figure 3 shows the mean surface brightness profiles from the smoothed images of the nine model LAEs in our analysis. The overall mean of the nine profiles is plotted in black. For each LAE, the central profile (e.g., $R \lesssim 15$ kpc) is largely determined by the smoothing kernel (point spread function; PSF). The peak surface brightness at the center shows a small variation among the nine individual profiles, around $(1-3) \times 10^{-17} \text{ erg s}^{-1} \text{ cm}^{-2} \text{ arcsec}^{-2}$.

At large projected radii, each LAE shows an extended profile, which can be identified as the diffuse LAH. The profile at large radii is much flatter than the central part. The surface brightness level of this extended component displays a substantial variation among the nine individual LAEs, as large as two orders of magnitude.

In the right panel of Figure 3, we compare the overall mean profile of the nine model LAEs with the one derived by Momose et al. (2014) from stacking the Ly α images of 316 $z \sim 3.1$ LAEs. According to Momose et al. (2014), the data at $R \lesssim 40$ kpc are reliable, while at larger radii systematic effects in the stacking analysis become significant compared to the signal (see the top-middle panel in their Figure 8). We mark such a transition by using filled circles at $R \lesssim 40$ kpc and open circles at $R \gtrsim 40$ kpc for the data points. The shaded region around the mean model profile attempts to quantify the uncertainty. The upper (lower) boundary is derived by excluding the LAE with the lowest (highest) surface brightness and averaging over the other eight LAEs. This serves to only provide some rough idea on the variation level of the mean profile, given the small number of model LAEs in our analysis.

On small scales ($R \lesssim 15$ kpc), the model profile matches the observed profile extremely well, which is striking. At first glance one may attribute this to coincidence, since we do not intend to fit the observed profile and we do not have any free parameters to adjust in

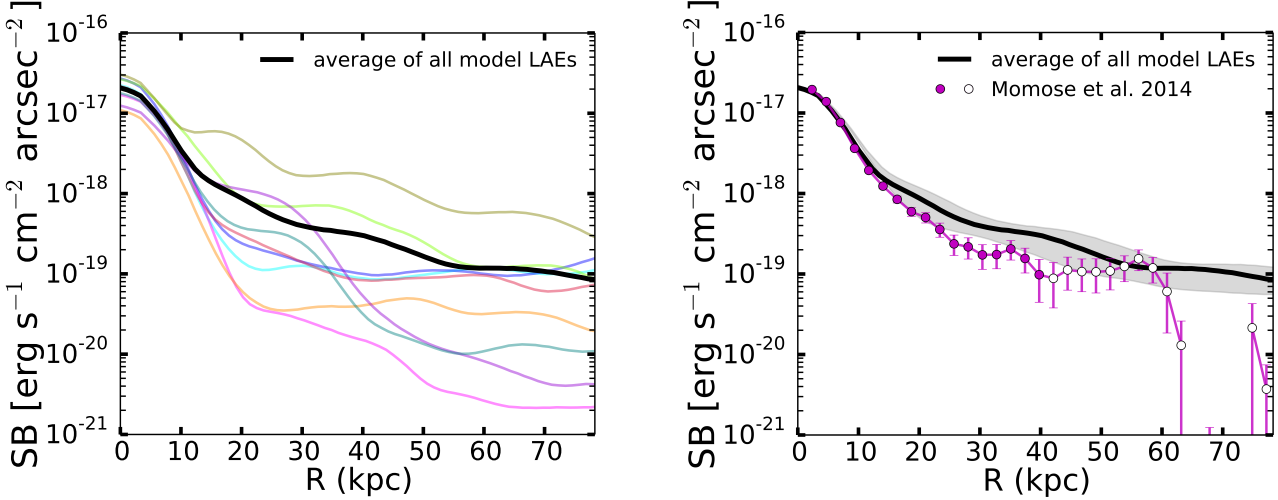


FIG. 3.— Ly α surface brightness profiles for the model LAEs in our analysis. *Left:* Ly α surface brightness profiles for individual model LAEs, with the average over all nine LAEs shown as the black curve. While the nine LAEs have similar surface brightness levels at small radii, they display large variations at large radii, reflecting the differences in gas distributions in our model halos. *Right:* Comparison of the average Ly α profile with observational results in Momose et al. (2014). Beyond ~ 40 kpc systematic effect in the image stacking analysis becomes important, indicated by the open circles. The shaded region attempts to give an idea of the spread in the model profile, obtained by excluding the LAE with the faintest or the brightest extended profiles.

our model. We directly use the Ly α emissivity and gas distribution in the simulation. The only two changes we apply in the model besides the radiative transfer calculation are “effective” dust and IGM absorption. The “effective” Ly α extinction optical depth is the same as the one adopted in Cen & Zheng (2013) for studying LABs, which suppresses the initial intrinsic Ly α emission. It aims at accounting for any uncertainties in the galaxy formation simulation. We tie it to the star formation rate and the relation is fixed by considering halos above $10^{12} M_{\odot}$ in Cen & Zheng (2013). We apply a mean absorption (scattering) for Ly α photons escaping the grid from the IGM outside of the simulation box.

In Cen & Zheng (2013), the observed Ly α luminosity-size relation of LABs and the Ly α luminosity function of LABs are reproduced by our radiative transfer modeling. So it may not be too surprising that the similar model also provides a good match to the Ly α emission in lower mass halos ($10^{11.5} M_{\odot}$). Since the surface brightness profile at the central part is largely determined by the PSF, the agreement with the observation means that the central Ly α luminosity in our model happens to be similar to the average luminosity of the 316 LAEs in the stacking analysis in Momose et al. (2014), which by all means is an encouraging sign.

At larger radii ($R \gtrsim 15$ kpc), the model curve is slightly higher (at a factor of two level) than the observation. Given the small number of LAEs and the lack of adjustment in the model, the agreement to the observation still appears remarkable, in particular if the uncertainties in the data points and in the model curve are taken into account (keeping in mind that the data may suffer from significant systematic bias at $R \gtrsim 40$ kpc). Both the shape and extent of the LAH are reasonably reproduced.

As a whole, our model mean Ly α surface brightness profile, effectively computed from stacking Ly α images of nine LAEs viewed along many different directions, shows good agreement with stacking analysis from ob-

served $z \sim 3.1$ LAEs, from the central part to the diffuse LAH extended to ~ 80 kpc. We proceed to investigate the contributions from various components to the surface brightness profile to gain more insights.

3.2. Decomposing the Ly α Surface Brightness Profile

We record the initial position of each photon, which makes it possible to separate the contributions to the surface brightness profile from photons originating at different places in our simulation.

In each halo, there is a central LAE with strong Ly α emission. We attribute Ly α photons launched within 10kpc of the halo center to the central LAE. There are also a few regions in the halo with high Ly α emissivity, which are small star-forming galaxies around the central LAE. In the Ly α images shown in Figure 2, such regions appear as relatively isolated peaks with surface brightness above $\sim 10^{-19} \text{ erg s}^{-1} \text{ cm}^{-2} \text{ arcsec}^{-2}$. The majority of them are below the detection threshold for typical LAE surveys, as is the case in Momose et al. (2014). In three of the nine LAEs, a few of the high emissivity regions can reach the detection threshold, and would show up as isolated LAEs around the central LAEs. We refer to the high emissivity regions as “knots” and associate to each knot Ly α photons launched within 10kpc of its center. Photons that belong to neither the central LAE nor the knots are identified as being emitted from the background of the simulation box. Most of them come from small clumps of gas that possess low rates of star formation. Clearly the distinction between the knots and the background depends on our choice, which can be arbitrary. However, our separation here serves the purpose of obtaining a rough idea on how Ly α photons from different physical regions contribute to the surface brightness profile.

The left panel of Figure 4 shows the decomposition of the mean surface brightness profile (black) into contributions from Ly α photons originating in the central

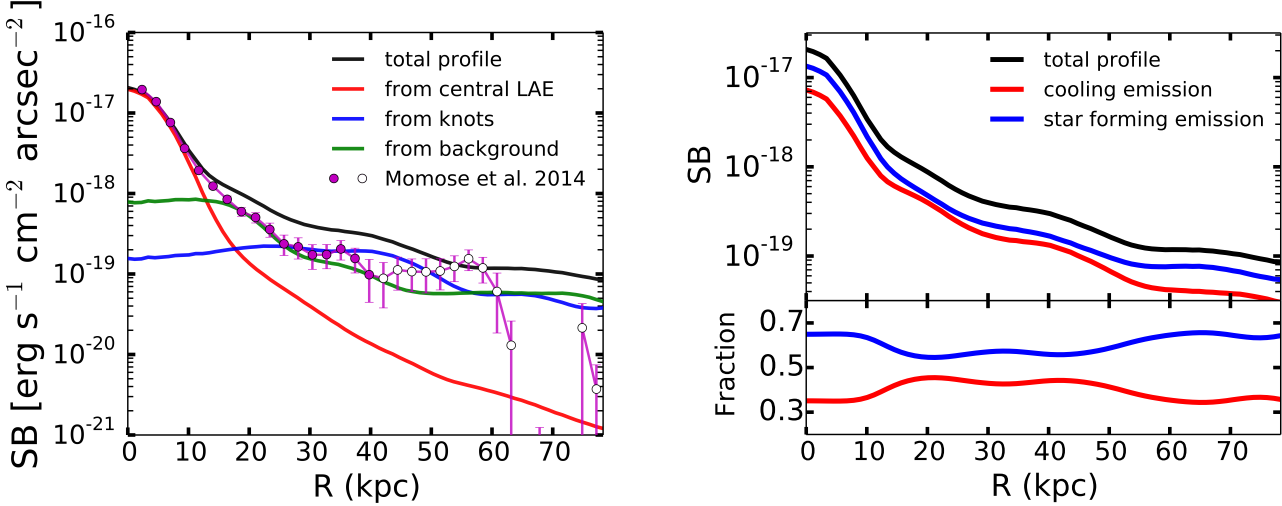


FIG. 4.— Decomposition of the total Ly α surface brightness profile into different components of Ly α emission. *Left:* The decomposition of the total profile into contributions from the central LAE (red curve), other high emission knots (blue curve), and background regions (green curve). Observational data from Momose et al. (2014) is shown in purple. Systematic bias is important for $R \gtrsim 40$ kpc, indicated by the open circles. Note that at radii larger than ~ 10 kpc, the profile from the central LAE is unable to account for observations, with the knot and background profiles playing dominant roles. *Right:* The decomposition of the total profile into contributions from star formation and cooling emission. The top panel shows profiles for each emission type, given in surface brightness units of $\text{erg s}^{-1} \text{cm}^{-2} \text{arcsec}^{-2}$. Star forming emission is shown in blue, and cooling emission is shown in red. The bottom panel shows the fractional contribution that each emission type makes to the total profile.

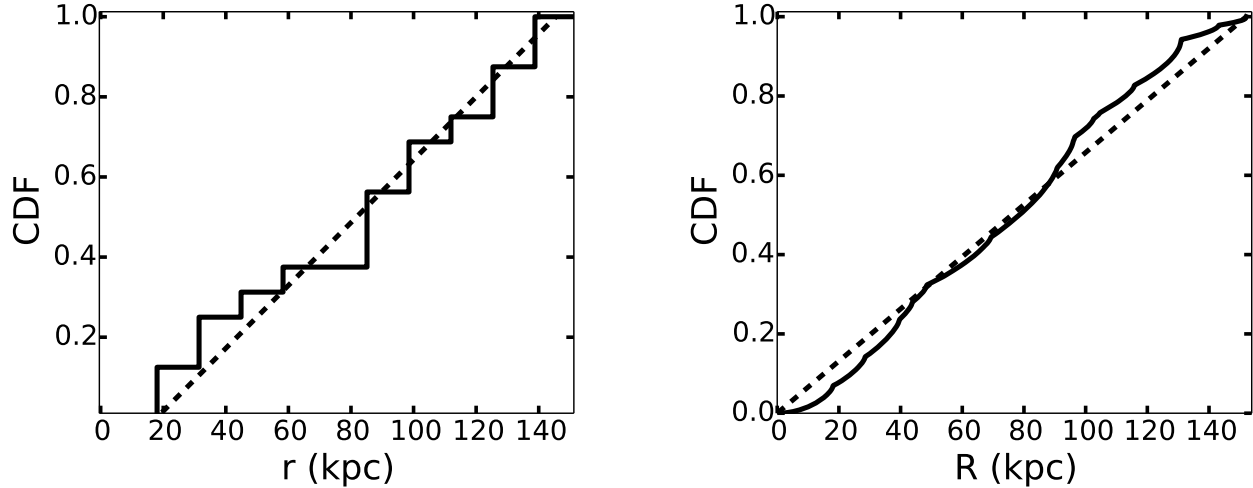


FIG. 5.— Spatial distribution of the identified high emission knots in our simulation. *Left:* The distribution of 3D distances of the knots to the box center. The solid line shows a cumulative distribution function (CDF) of the 3D distances, with the dashed curve corresponding to a number density profile $n(r) = 0$ for $r < 20$ kpc and $n(r) \propto r^{-2}$ for $r \geq 20$ kpc. *Right:* The distribution of 2D projected distances of the knots to the box center. The solid line shows the CDF of the 2D distances and the dashed curve is for a number density distribution $\propto R^{-1}$.

LAE (red), the knots regions (blue), and the background regions (green).

After the radiative transfer, Ly α photons originating from the central LAE appear to peak around the central region, following the PSF. The entire amplitude of the overall surface brightness profile at $R < 10$ kpc comes from this component. The scatterings of photons with neutral hydrogen atoms in the circumgalactic and intergalactic media lead to an extended profile beyond ~ 15 kpc. The profile drops toward large radii, roughly

following $R^{-3.3}$, which is too steep to account for the LAHs seen in both the model and observations.

Ly α photons from the knots and background regions make comparable contributions (within a factor of about two) to the overall surface brightness profile at scales above ~ 20 kpc. They have similar profiles, which in turn are similar to that of the LAH and are flatter than the extended profile from scattered photons from the central LAE. Together, they dominate the profile at $R \gtrsim 20$ kpc.

The above decomposition leads to the interesting im-

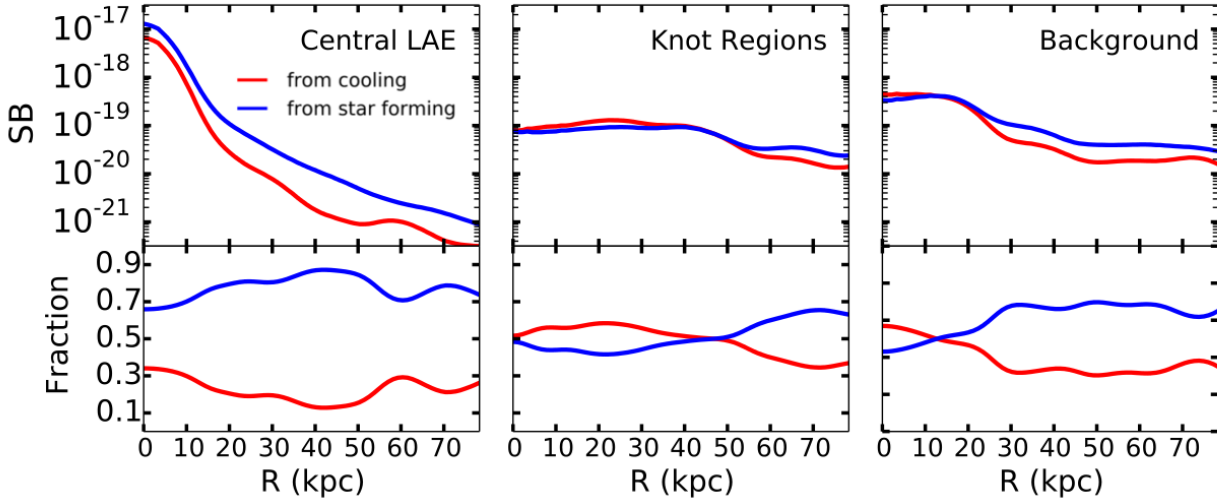


FIG. 6.— A further decomposition of the averaged surface brightness profile into contributions from star formation (blue curves) and cooling radiation (red curves). From left to right, the panels show profiles for photons produced within 10kpc of the central LAEs, within the knot regions, and from the background areas. The top panels show surface brightness in units of $\text{erg s}^{-1} \text{cm}^{-2} \text{arcsec}^{-2}$, while the bottom panels show the relative contributions.

plication that the observed extended Ly α emission of LAHs is largely caused by emission from regions of low star formation rates spatially distributed inside the host dark matter halos of the central LAEs, and that photons diffusing out from the central LAE as a result of the radiative transfer process play only a secondary role in producing the observed extended emission.

Because the identified high-emission knots contribute significantly to the surface brightness profile at large radii, it is important to examine their spatial distribution. The left panel of Figure 5 shows the cumulative distribution function (CDF) of the 3-dimensional (3D) distance r from the knots to the center for all the nine LAEs. Since we define the radius of each knot region and the central LAE to be 10 kpc, any high-emission areas within 20 kpc of the center will not be identified as independent knots in our analysis. Therefore, the CDF curve starts at $r = 20$ kpc. The dashed curve corresponds to a number density distribution $n(r) \propto r^{-2}$ (for $r \geq 20$ kpc and 0 for $r < 20$ kpc). The plot shows that the high-emission knots closely follow a singular isothermal distribution up to at least $\sim 3R_{\text{vir}}$.

As we study the surface brightness profile, it would be more illustrative to examine the projected distribution of the knots. For this purpose, we chose a large number of isotropically distributed viewing directions. For each viewing direction and each LAE, we record the projected radius to the center for each knot. The right panel of Figure 5 shows the CDF for the 2D projected radii R . The dashed curve is the CDF for a surface number density that follows R^{-1} , which appears to be a reasonable description of the distribution of knots. This is consistent with the CDF of the 3D radii. The distribution of knots explains the shallow slope in the mean surface brightness profile seen in the model or observed LAHs (e.g., Figure 3 and Figure 4), which has a slope around -1 .

We also decompose the surface brightness profile into contributions from Ly α photons generated by star formation and cooling radiation, as shown in the right panel

of Figure 4. The profiles from the two contributions are similar, but the photons from cooling radiation always sub-dominant, making about 30-40% of the total Ly α light in the extended LAHs.

Figure 6 shows the decomposition of our surface brightness profiles into contributions from star formation and cooling radiation for the central LAE, the identified knot regions, and the background. For Ly α photons produced in the central LAE, cooling radiation makes up about 1/3 of the observed Ly α emission near the center, and its contribution drops to 15% at $R \sim 20$ kpc. For Ly α photons produced in the knot regions, cooling radiation and star formation contributions are comparable, and for those produced in background, the star formation contribution dominates. The latter two components depend on how we define knot regions. If we choose a lower threshold to define knots, star formation would become the dominant mechanism in producing Ly α photons in knot regions.

3.3. Constraints from the UV Surface Brightness Profile

The Ly α surface brightness profile from our model shows an encouraging agreement with the data. Besides Ly α , the stacking analysis is also performed for UV images (e.g., Momose et al. 2014). UV photons are produced from star formation. Unlike Ly α photons, they do not interact with neutral hydrogen through resonant scattering. So they escape directly from their point of creation (modulated by dust extinction), which allows them to serve as a tool to map out regions of star formation. The UV profile of LAEs can therefore provide complementary information about LAHs and can be used to further constrain the origin of LAHs.

We convert the SFR to UV luminosity (at rest-frame 1500Å) using the prescription $L_{\text{UV}} = 8 \times 10^{27} [\text{SFR}/(M_{\odot} \text{yr}^{-1})] \text{erg s}^{-1} \text{Hz}^{-1}$ (Madau et al. 1998; Zheng et al. 2010). It assumes a Salpeter initial mass function of stars and solar metallicity. While a dust extinction should be included to obtain the observed UV

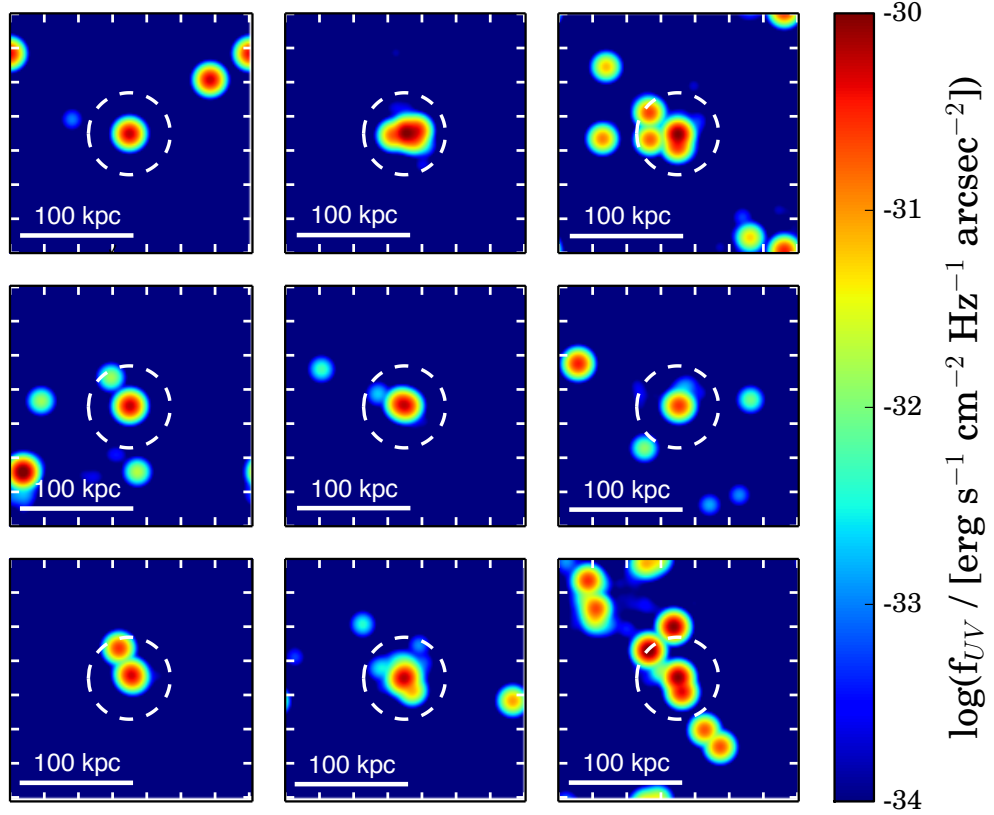


FIG. 7.— UV surface brightness images for all nine model LAEs in our original analysis. Each image is 224 kpc (physical) on a side and has been smoothed by a 2D Gaussian kernel with a FWHM of $1.32''$ to match the observation setup. The dashed circle in each panel has a radius of 40 kpc, roughly corresponding to the radius that systematic effects become important in the stacking analysis in (Momose et al. 2014). The observed profile can put strong constraints on the clustered UV sources around the central galaxies, as discussed in the text.

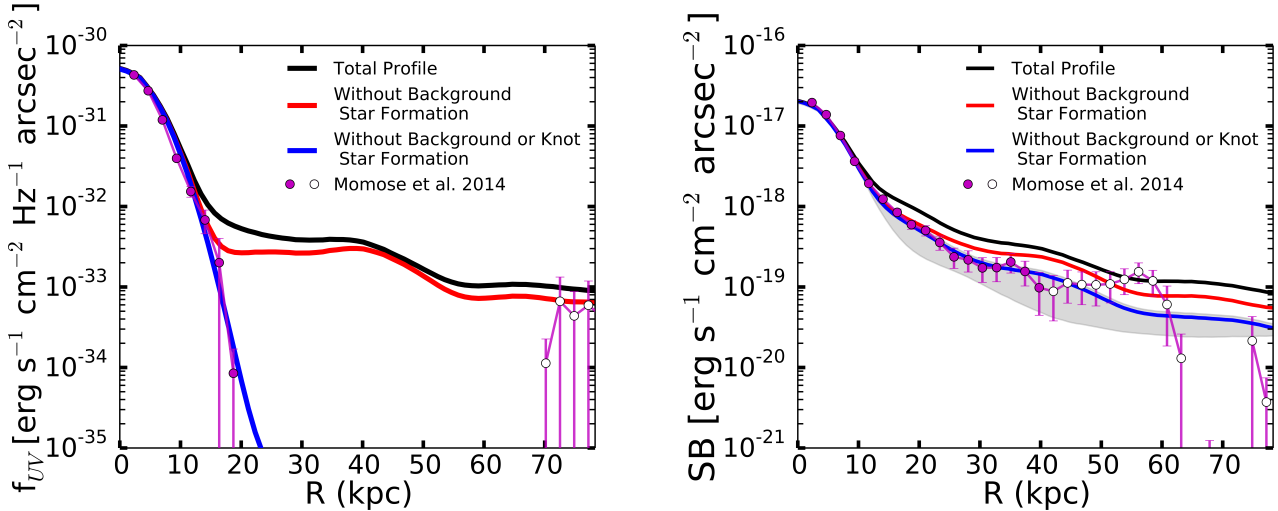


FIG. 8.— Average UV and Ly α surface brightness profiles and the effect of star formation in the outer halo. *Left:* Comparison of model UV profiles with observation. The black curve is the average profile from our initial model. The red curve shows the profile after removing star formation from the background areas in halo, and the blue curve shows the profile after removing all star formation in the outer halo, which matches the observed UV profile (data points) well. *Right:* The corresponding changes in the model Ly α profile. In each panel, observational data are taken from Momose et al. (2014) with open circles representing the region where the data starts to be limited by systematics. The gray shaded region in the right panel gives an idea of the spread of the profile, obtained by excluding the LAE with the faintest or the brightest extended profiles from the average.

luminosity, it is degenerated with the above assumption about the stellar population. For example, a sub-solar metallicity plus dust extinction would lead to a similar conversion factor. Given such an uncertainty in the model, we simply adopt the above conversion to proceed. We create UV photons based on the SFR in each cell and assign a random escape direction for each photon. Figure 7 displays the UV images of the nine model galaxies observed along the same direction as in Figure 2. Noticeably, in these original images without modifications of the model, there are star-forming regions within the halos around the central galaxies, whose existence can be strongly constrained by the data as we will show.

To study the average UV light distribution seen in the stacking analysis, we follow the method described in § 2.2 to produce the average UV surface brightness profile for each model LAE.

The black curve in the left panel of Figure 8 shows the UV profile predicted by the model. At small radii ($R \lesssim 15\text{kpc}$), the model curve is almost right on top of the observed profile. Such a coincidence indicates that our SFR-to-UV conversion factor is about right in reflecting a combined effect of stellar population, extinction, and model SFR, even though there are uncertainties in each component. The model reproduces the central UV luminosity, and the shape of the profile simply follows that of the PSF.

At large radii ($R \gtrsim 15\text{kpc}$), the model shows an extended UV halo (left panel of Figure 8). This is not unexpected, given that emission produced from star formation in the outer halo makes a substantial contribution to the extended Ly α profile (Figure 6). However, this is in apparent contrast with observations (Momose et al. 2014). Little evidence is shown for such extended UV halos (see the data points in the left panel of Figure 8). Given the noise level in the observation, the model UV profile at large radii is about two orders of magnitude higher than the observed profile. Clearly, to reconcile the large difference between the model and observation, star formation contribution to the model UV profile in the outer halo needs to be suppressed.

The extended UV emission comes from the star forming component of the knot and background regions, which are associated with star formation in satellite galaxies or tidally stripped materials around the central LAE. One possible way of suppressing this component of UV emission is to invoke higher dust extinction in satellite galaxies and stripped materials than in the central LAE. Being clearly contrived, this proposal needs the extinction in the outer halo regions to be about 100 times (5 magnitudes) higher than in the central LAE to explain the relative amplitude of the UV surface brightness at small and large radii. In addition, the absorbed UV photons would be reprocessed into infrared emission, leading to an extended infrared halo. We regard the above explanation to be unlikely.

A more probable explanation is that the star formation recipe in the galaxy formation simulation may have over-produced stars in the outer halos. If we remove emission from star formation in the background regions (leaving only cooling radiation in our background profile), the situation does not improve much (see the red curve in the left panel of Figure 8). We find that only by removing the majority of star formation from the outer halo (including

both the knot and background regions) are we able to make the model UV profile (blue curves) consistent with the observed one in Momose et al. (2014). If we take the level of the observed UV surface brightness beyond 70 kpc for a conservative estimate, about 90% of the star formation in the outer halo needs to be removed from the model in order to match the observed UV profile.

Removing star formation from these regions also effects the Ly α profile. The right panel of Figure 8 shows the response of the Ly α profile to the above changes. The effect is not drastic, and the Ly α profile for the case of removing all star formation in the outer halo (blue curve) drops to a level in surprisingly much better agreement with observations. With this prescription, we are able to find the average component contributions to the total Ly α luminosity within projected radius $R < R_{\text{vir}} = 56\text{kpc}$ — 45% from star formation in the central galaxy, 20% from cooling radiation within and around the central galaxy ($r < 10\text{kpc}$), and 35% from cooling radiation in the outer halo. Therefore, on average cooling radiation can contribute to about half of the total Ly α luminosity in such halos. The diffuse LAH, which mainly results from the cooling radiation in the outer halo, makes up about 1/3 of the total emitted Ly α luminosity, consistent with the result in Momose et al. (2014).

We see that the UV profile, in combination with the Ly α profile, can greatly help constrain the nature of the LAHs. Our investigation implies that cooling radiation in the outer halo may play a significant role in forming extended Ly α halos. The caveats and more discussions are presented in the next section.

4. SUMMARY AND DISCUSSION

We perform Ly α radiative transfer modeling of $z = 3.1$ LAEs with a high resolution hydrodynamic galaxy formation simulation to study the extended Ly α -emitting halos recently discovered in observation from image stacking analysis. We develop a method to compute the mean surface brightness profile from averaging over many different viewing directions. We consider nine model LAEs residing in halos of $10^{11.5} M_{\odot}$ and find their mean Ly α surface brightness profile to be in remarkable agreement with the observed profile in Momose et al. (2014), at both the central and extended parts.

To investigate the origin of the extended Ly α emission, we decompose the profile into contributions from Ly α photons produced in different regions, which include the central LAE in each simulation box, dense regions of high star formation activity spatially separated from the central LAE (dubbed as “knots”), and faint background areas. The latter two outer halo components are associated with satellite galaxies or tidally stripped materials in the halo. We find that Ly α photons originating from the central LAE but scattered to large radii by hydrogen atoms in the circumgalactic gas produce an extended profile that is too low in surface brightness to account for the observed LAH. Ly α emission from the outer halo can explain the extended LAH. Without adjusting any parameters, the extended Ly α profile in our model agrees with the observed one remarkably well.

Ly α emission from the outer halo has two components — gravitational cooling radiation and emission from star formation. In the simulation, we find that star formation dominates, although cooling radiation makes a substan-

tial contribution. With the star formation contribution, the model predicts the existence of extended UV halos around LAEs, which is about 100 times brighter than seen in observation. This causes an apparent tension, even though the central UV profile from our model agrees well with the observed one. Conversely, the UV profile can tighten the constraints on the origin of the LAHs and put stringent tests on the galaxy formation model. Our result suggests that the star formation in the outer halo may have been over-predicted in the simulation by a factor of ten or more. Only by removing most of the star formation emission from the outer halo in the model can we reproduce the observed UV profile with no substantial extended emission. By doing so, the extended Ly α profile becomes even better reproduced, agreeing with the observed one surprisingly well, with the contribution to our profile at larger radii coming from cooling radiation in the outer halo.

Taken at face value, our investigation shows that suppressing the star formation in the outer halo but keeping the cooling radiation can explain both the observed Ly α and UV profiles of LAEs in Momose et al. (2014), from small radii ($\lesssim 15$ kpc) to large radii (up to ~ 80 kpc). The agreements between the model and data are excellent. This is remarkable, especially given that we do not intend to fit the profiles by tuning parameters. With this scenario of our model, we find that the cooling radiation can contribute to about half of the total Ly α luminosity within projected radius $R < R_{\text{vir}}$, where $R_{\text{vir}} = 56$ kpc ($\sim 7.2''$) is the virial radius of the LAE host halo. The diffuse LAH from the cooling radiation in the outer halo, which is usually buried in sky noise for individual LAEs, makes about 1/3 of the above luminosity.

Are we really detecting cooling radiation in the extended LAHs? More studies are clearly necessary to answer this question.

Ly α photons originating near the halo center (from both star formation and cooling radiation) but scattered to large radii by the hydrogen atoms in the CGM do produce an extended Ly α halo, as predicted by, e.g., Laursen & Sommer-Larsen (2007) and Zheng et al. (2011b). However, our radiative transfer model with the high-resolution galaxy formation simulation shows that such a contribution alone is not able to explain the surface brightness level of the observed LAH (e.g., lower by a factor of 10 around $R = 40$ kpc). The exact profile of this component should depend on the density and velocity distribution of the circumgalactic gas. Some analytic models with clumpy CGM and decelerating outflows can produce scattered Ly α halos at the observed surface brightness level (e.g., Steidel et al. 2011; Dijkstra & Kramer 2012). It is worth investigating the contribution from such scattered halos with more realistic CGM distributions from high-resolution galaxy formation simulations with various prescriptions of the star formation feedback (e.g., Suresh et al. 2015; Muratov et al. 2015; Kimm et al. 2015).

We also need to figure out whether the galaxy formation simulation we use over-predicts the star formation in the outer halos. Adopting different star formation recipes or comparing different simulations would be helpful. If it turns out that the star formation in outer halos is reasonable, we need to come up with other solutions of suppressing the UV emission in outer halos. Such solutions

may result in extended halos in other bands (e.g., infrared). Observationally, stacking analysis in other bands also helps to pin down the nature of LAHs. Instead of suppressing the UV radiation in satellite galaxies, another interesting possibility is to suppress the formation of satellites, e.g., by reducing the small-scale power of the primordial matter density fluctuation.

Gravitational cooling radiation from accretion of gas is a process expected to occur during galaxy formation, mainly in the form of Ly α emission from collisional excitation and de-excitation of hydrogen atoms in gas around 2×10^4 K (e.g., Fardal et al. 2001). Many previous studies of cooling radiation with hydrodynamical simulations focus on investigating it as a possible mechanism to explain Ly α blobs (e.g., Fardal et al. 2001; Furlanetto et al. 2005; Yang et al. 2006; Goerdt et al. 2010; Faucher-Giguère et al. 2010), which are more luminous than LAHs (Steidel et al. 2000). As shown by Yang et al. (2006) and Faucher-Giguère et al. (2010), an accurate prediction of the cooling Ly α emission relies on an accurate treatment of the self-shielding effect for the ionizing photons, which affects the ionization and thermal states of the accreted gas. In the simulation used in this work, self-shielding correction is performed on-the-fly. There could be small variations in the predicted cooling radiation with different self-shielding correction method, but it is unlikely to remove the cooling radiation signal in our model.

One caveat to keep in mind is that our results in this paper are based on radiative transfer modeling of nine simulated galaxies in halos of $10^{11.5} M_{\odot}$. First, our analysis suffers from small number statistics. While we attempt to make full use of the nine galaxies by obtaining the mean surface brightness profile from averaging all viewing angles (effectively creating a much larger sample for stacking), modeling more galaxies definitely helps the study of LAHs. More galaxies are also needed to explore the dependence of LAHs on the properties of galaxies and their environments (e.g., Matsuda et al. 2012). Second, the mass of halos ($10^{11.5} M_{\odot}$) considered in this work seems to be on the high end of LAE-hosting halos. The LAE halo masses inferred from clustering analysis are typically $10^{11 \pm 1} M_{\odot}$ (Ouchi et al. 2010). Clearly it is necessary to investigate how the Ly α and UV surface brightness profiles and their decomposition into cooling and star forming components varies with halo mass. As an example of the potential impact of halo mass, Rosdahl & Blaizot (2012) find that the extent of cooling radiation in the outer halo is dependent on halo mass, resulting from a positive correlation between the efficiency of cold streaming accretion and halo mass. Additional radiative transfer modeling of galaxies in lower mass halos comparing emission the central LAE with star formation and cooling radiation in the outer halo will elucidate to what extent our results in this paper hold.

We plan to carry out studies related to the above aspects and the redshift evolution of LAHs for a better understanding of the origin and for using LAHs to learn about the CGM and galaxy formation.

E.L., Z.Z., and R.S. are supported by NASA grant NNX14AC89G and NSF grant AST-1208891. The support and resources from the Center for High Performance Computing at the University of Utah are grate-

fully acknowledged. Computing resources were in part provided by the NASA High-End Computing (HEC) Program through the NASA Advanced Supercomputing (NAS) Division at Ames Research Center. R.C. is supported in part by grants NASA NNX11AI23G

and NNX12AF91G. This work was supported by World Premier International Research Center Initiative (WPI Initiative), MEXT, Japan, and KAKENHI (23244025) Grant-in-Aid for Scientific Research (A) through Japan Society for the Promotion of Science (JSPS).

REFERENCES

Brinchmann, J., Charlot, S., White, S. D. M., et al. 2004, MNRAS, 351, 1151

Bryan, G. L., & Norman, M. L. 2000, Institute for Mathematics and Its Applications, 117, 165

Cen, R. 2011, ApJ, 742, L33

—. 2012, ApJ, 748, 121

Cen, R., & Zheng, Z. 2013, ApJ, 775, 112

Dijkstra, M., & Kramer, R. 2012, MNRAS, 424, 1672

Fardal, M. A., Katz, N., Gardner, J. P., et al. 2001, ApJ, 562, 605

Faucher-Giguère, C.-A., Kereš, D., Dijkstra, M., Hernquist, L., & Zaldarriaga, M. 2010, ApJ, 725, 633

Feldmeier, J. J., Hagen, A., Ciardullo, R., et al. 2013, ApJ, 776, 75

Furlanetto, S. R., Schaye, J., Springel, V., & Hernquist, L. 2005, ApJ, 622, 7

Fynbo, J. P. U., Ledoux, C., Möller, P., Thomsen, B., & Burud, I. 2003, A&A, 407, 147

Gawiser, E., Francke, H., Lai, K., et al. 2007, ApJ, 671, 278

Goerdt, T., Dekel, A., Sternberg, A., et al. 2010, MNRAS, 407, 613

Guaita, L., Gawiser, E., Padilla, N., et al. 2010, ApJ, 714, 255

Jeeson-Daniel, A., Ciardi, B., Maio, U., et al. 2012, MNRAS, 424, 2193

Jiang, L., Egami, E., Fan, X., et al. 2013, ApJ, 773, 153

Joung, M. R., Cen, R., & Bryan, G. L. 2009, ApJ, 692, L1

Kimm, T., Cen, R., Devriendt, J., Dubois, Y., & Slyz, A. 2015, arXiv:1501.05655

Laursen, P., & Sommer-Larsen, J. 2007, ApJ, 657, L69

Madau, P., Pozzetti, L., & Dickinson, M. 1998, ApJ, 498, 106

Matsuda, Y., Yamada, T., Hayashino, T., et al. 2012, MNRAS, 425, 878

Muratov, A. L., Keres, D., Faucher-Giguere, C.-A., et al. 2015, arXiv:1501.03155

Momose, R., Ouchi, M., Nakajima, K., et al. 2014, MNRAS, 442, 110

Ouchi, M., Shimasaku, K., Akiyama, M., et al. 2008, ApJS, 176, 301

Ouchi, M., Shimasaku, K., Furusawa, H., et al. 2010, ApJ, 723, 869

Partridge, R. B., & Peebles, P. J. E. 1967, ApJ, 147, 868

Rhoads, J. E., Dey, A., Malhotra, S., et al. 2003, AJ, 125, 1006

Rosdahl, J., & Blaizot, J. 2012, MNRAS, 423, 344

Schaerer, D., & Verhamme, A. 2008, A&A, 480, 369

Steidel, C. C., Adelberger, K. L., Shapley, A. E., et al. 2000, ApJ, 532, 170

Steidel, C. C., Bogosavljević, M., Shapley, A. E., et al. 2011, ApJ, 736, 160

Suresh, J., Bird, S., Vogelsberger, M., et al. 2015, arXiv:1501.02267

Tasitsiomi, A. 2006, ApJ, 645, 792

Verhamme, A., Schaerer, D., Atek, H., & Tapken, C. 2008, A&A, 491, 89

Yang, Y., Zabludoff, A. I., Davé, R., et al. 2006, ApJ, 640, 539

Zahid, H. J., Yates, R. M., Kewley, L. J., & Kudritzki, R. P. 2013, ApJ, 763, 92

Zheng, Z., Cen, R., Trac, H., & Miralda-Escudé, J. 2010, ApJ, 716, 574

—. 2011a, ApJ, 726, 38

Zheng, Z., Cen, R., Weinberg, D., Trac, H., & Miralda-Escudé, J. 2011b, ApJ, 739, 62

Zheng, Z., & Miralda-Escudé, J. 2002, ApJ, 578, 33

Zheng, Z., & Wallace, J. 2014, ApJ, 794, 116